Permeability evolution in carbonate fractures: Competing roles of confining stress and fluid pH

Takuya Ishibashi,[1] Thomas P. McGuire,[2] Noriaki Watanabe,[1] Noriyoshi Tsuchiya,[1] and Derek Elsworth[2]

[1] We explore the permeability evolution of fractures in carbonate rock that results from the effects of mechanical stress and nonequilibrium chemistry (pH of fluid). Core plugs of Capitan limestone are saw cut to form a smooth axial fracture that is subsequently roughened to simulate a natural fracture with controlled surface topography. Aqueous solutions of ammonium chloride (pH 5~7) transit these plugs at confining stresses of 3–10 MPa, with flow rates and mineral mass fluxes measured to constrain competing mechanisms of permeability evolution. The effluent calcium concentrations are always much lower than equilibrium calcium solubility, resulting in the dissolution-dominant permeability evolution in our experiments. Depending on the combination of confining stress and fluid pH, the fracture apertures either gape (permeability increase) or close (permeability reduction). We quantitatively constrain the transition between gaping (pH < 6.1) and closing (pH > 6.5) with this transition independent of confining stress up to 10 MPa. A transitional regime (6.1 < pH < 6.5) of invariant aperture represents a balance between the two mechanisms of free-face dissolution and pressure solution at the bridging asperities. We employ a lumped-parameter model to interpret the dissolution-dominant evolution of permeability. By considering different dissolution rate constants between noncontacting asperities and the stagnant water film at the contacting asperities, this model replicates the principal characteristics of permeability evolution of the fracture. Observed rates of aperture change are ill matched when the influent pH is 5–6, since wormhole formation is not accommodated in the model. These observations offer a promising pathway to index the switch from aperture gaping to aperture closing for reactive flow as reactivity is reduced and stress effects become more important.

1. Introduction

[2] An understanding of the flow and transport characteristics through rock fracture networks is of critical importance in many engineering and scientific applications. These include effective recovery of targeted fluids such as oil/gas, geothermal, or potable waters, and safe isolation of hazardous materials. The significant role of mechanical and nonequilibrium chemical effects on permeability evolution of fracture networks is clear [*Tsang*, 1991; *Manga et al.*, 2012]; however, the interaction of these competing processes remains poorly understood.

[3] The evolution of fracture permeability is generally influenced by multiple parameters that include variability of initial apertures [*Hanna and Rajaram*, 1998; *Durham et al.*, 2001; *Nemoto et al.*, 2009], mineral composition of the fracture surfaces [*Gouze et al.*, 2003; *Noiriel et al.*, 2007], and advective-diffusive transport of dissolved minerals [*Detwiler et al.*, 2003; *Szymczak and Ladd*, 2004; *Detwiler and Rajaram*, 2007]. These effects are suggested through experimental and numerical studies. Additionally, the formation of wormholes, which is widely recognized within porous system [*Panga et al.*, 2005; *Kalia and Balakotaiah*, 2009], also exerts a significant impact on the evolution of fracture permeability [*Polak et al.*, 2004; *Liu et al.*, 2006; *Szymczak and Ladd*, 2009].

[4] In order to constrain hydrologic models for fractured carbonate reservoirs or for natural karst systems, we explore the evolution of permeability in carbonate fractures in this work. Fractures in carbonates are particularly influenced by the mechanical, chemical, and hydrological effects due to the high relative solubility of calcite. In particular, permeability reduction is driven as bridging asperities are removed by stress-enhanced dissolution or as secondary minerals are reprecipitated (i.e., pressure solution). Anomalous reduction

[1] Graduate School of Environmental Studies, Tohoku University, Aoba-ku, Sendai, Japan.

[2] Department of Energy and Mineral Engineering, Center for Geomechanics, Geofluids, and Geohazards, EMS Energy Institute, Pennsylvania State University, University Park, Pennsylvania, USA.

Corresponding author: T. Ishibashi, Graduate School of Environmental Studies, Tohoku University, 6-6-20 Aramaki-aza-Aoba, Aoba-ku, Sendai 980–8579, Japan. (tishibashi@geo.kankyo.tohoku.ac.jp)

in permeability has been reported in some instances at modest temperatures (50°C–150°C) [*Polak et al.*, 2003] and low effective stresses (0.2 MPa) and also with acidic solutions [*Durham et al.*, 2001]. Conversely, increases in permeability may be driven by the etching of the fracture void by dissolution (i.e., free-face dissolution). Permeability increase in natural fractures has been observed in carbonate reservoirs [*Liu et al.*, 1997] and in the natural development of karst [*Palmer*, 1991]. These two opposing behaviors operate concurrently, with varying strengths, resulting in permeability evolution that may spontaneously switch in the sense as the dominant mechanism switches [*Polak et al.*, 2004]. Lumped-parameter models capable of describing this behavior of spontaneous switching have been developed [*Liu et al.*, 2006; *Yasuhara et al.*, 2006a, 2006b].

[5] However, to date a conclusive view of permeability evolution in carbonate fracture has not evolved to define response a priori for arbitrary confining stresses and reactive chemistry of the fluid—specifically whether fracture permeability will increase or decrease under net dissolution. Without reliable predictions of permeability evolution in a single fracture, we cannot project the spatial- or temporal evolution of the fracture network. Thus, the key purpose of this paper is to define the comprehensive factors that control the ensemble behavior.

[6] In this study, we focus on the competition between mechanical and nonequilibrium chemical effects on the evolution of permeability in fractures. This experimental and analytical study investigates the change in fluid-flow characteristics within carbonate fractures, where chemical effects are significant, for various combinations of confining stress and pH of the fluid. Measurements of the evolution of fracture permeability are used to constrain lumped-parameter models of free-face and pressure-induced dissolution that contribute to changes in fracture porosity.

2. Experimental Method

[7] We conduct carefully controlled experiments to measure flow rate and dissolved mineral mass fluxes in fractured samples permeated by reactive fluid under stress. Flow rates and dissolved mass fluxes are used to assign independent constraints to permeability evolution, described later.

2.1. Sample Preparation

[8] Flow-through experiments are conducted on cylindrical cores (25 mm in diameter and ∼50 mm in length) of Capitan massive limestone (from the Guadalupe Mountains in New Mexico). This limestone is from the Permian Capitan reef [*King*, 1948] and comprises a fine-grained light-gray low-porosity (<1%) matrix containing isolated vugs (<3mm). Here, four different scales of cores were prepared (Table 1). These cores are prefractured by sectioning the samples along their cylindrical axis by a rock saw. The planar fracture surfaces are uniformly roughened with "60 grit" (423 μm) abrasive compound to yield a controlled fracture roughness. The samples are reabraded after each experiment to create a statistically repeatable roughness. The appearances of these fracture surfaces are shown in Figure 1. In these figures, the black voids on the surfaces show the locations of isolated vugs originally present

Table 1. Sample Sizes Used in the Experiments

Sample Number	Diameter (mm)	Length (mm)
TD 01	25	51
TD 02	25	51
TD 03	25	40
TD 04	25	50

within the rock samples. Scanning electron microscope (FEI Quanta 200) images (Figure 1e) indicate that the diameter of grains on the fracture surface is between 1 and 10 μm. The abrading is the same for all fractured rock samples used in our experiments, resulting in similar fracture surfaces. As a result, no distinct differences of fracture surface topography are observed by the white-light interferometry at the microscale. Note that surface profiling is not conducted in the present work. These cores are reused in multiple experiments by reabrading their surfaces after each flow-thorough experiment. The thickness of the layer removed in each abrading is greater than 200 μm and is therefore greater than the expected fluid diffusion distance into the rock matrix (∼100 μm) from the prior experiment. Each core sample is reused up to ∼10 times but with largely (statistically) reusable fracture surface topography.

### 2.2. Experimental System and Procedure for Flow-Through Experiment

[9] The arrangement for the flow-through system is shown in Figure 2. The upper and lower halves of the rock samples are mated and set between end platens. This assembly is placed within a latex sleeve and confined inside a triaxial pressure cell. The stainless steel platens are pierced by fluid supply lines and enable fluid transmission along the length of the core. An aqueous solution of ammonium chloride is used as the flowing fluid. The ammonium chloride controls the pH of the fluid according to the following reactions:

$$NH_4Cl \rightarrow NH_4^+ + Cl^-, \tag{1}$$

$$NH_4^+ + H_2O \leftrightarrows NH_3 + H_3O^+, \tag{2}$$
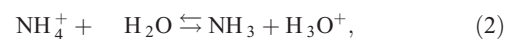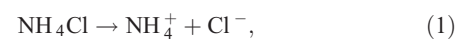
and the relationship between the theoretical pH value and the molarity of ammonium chloride is given by

$$pH = -\log_{10}\sqrt{C_{NH_4Cl} \cdot \left(\frac{K_w}{K_b}\right)}, \tag{3}$$

[10] where K_w is the ionization constant of water (1.0 × 10^{-8} mol² m⁻⁶), K_b is the base ionization constant of ammonia (1.74 × 10^{-2} mol m⁻³), and C_{NH_4Cl} is molarity of ammonium chloride [ML^{-3}]. The molarity is straightforwardly converted into the mass concentration by using the molar mass (5.35 × 10^{-2} kg m⁻³ for ammonium chloride). In this study, we prepare six different fluids with theoretical pH values of 5.0, 6.0, 6.1, 6.3, 6.5, and 7.0 by adjusting mass concentrations of ammonium chlorides shown in Table 2. Degassing is not conducted for these fluids. The pH values of these fluids are preliminarily measured by a pH meter beside the flow-through experiments (Table 2).
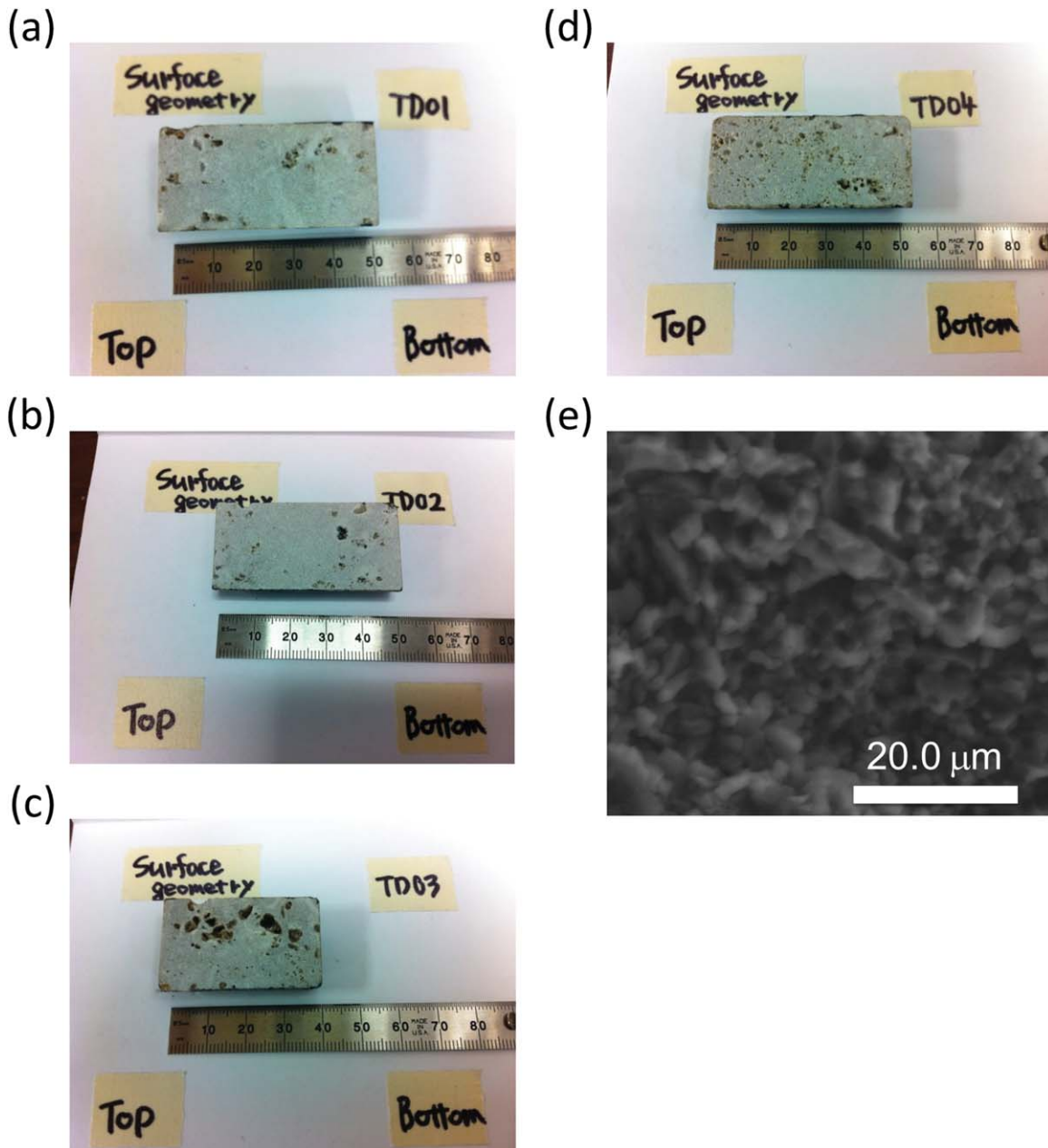
Figure 1. Surface topographies for artificial fractures in limestone for samples (a) TD01, (b) TD02, (c) TD03, and (d) TD04, and (e) SEM image for the fracture surface. Fluid is injected from "top" to "bottom" in the present study.

Measured pH values are slightly different from the theoretical pH values, but are of the correct order. Note that the net rate of calcite dissolution is strongly affected by the pH of the contacting fluid [*Plummer et al.*, 1978; *Chou et al.*, 1989]. Confining stress across the sample and differential fluid pressure along the sample fracture are established by gas drive controlled by a nitrogen tank. Flow along the sample is from an upstream reservoir to a downstream reservoir. Backpressure for the flow is prescribed at 600 kPa by a pressure regulator located with downstream reservoir. The inlet pressure of the upstream reservoir is set to 700, 800, or 900 kPa, resulting in a differential pressure of 100,

200, or 300 kPa. These differential pressures are measured by analog pressure gauges, which have a scale resolution of 20 kPa, during the flow-through experiments. A total of 18 experiments are run with constant inlet pH and for confining stresses of 3, 5, and 10 MPa. With the confining and differential pressure prescribed, fluid-flow rate through the fracture is measured every 20 min by weighing the effluent reservoir on an electronic balance at room temperature (298 K).

[11] Hydraulic aperture of the fracture averaged over 20 min of the experiment is recovered from the flow-rate measurements via the cubic law assumption [*Nemoto et al.*,
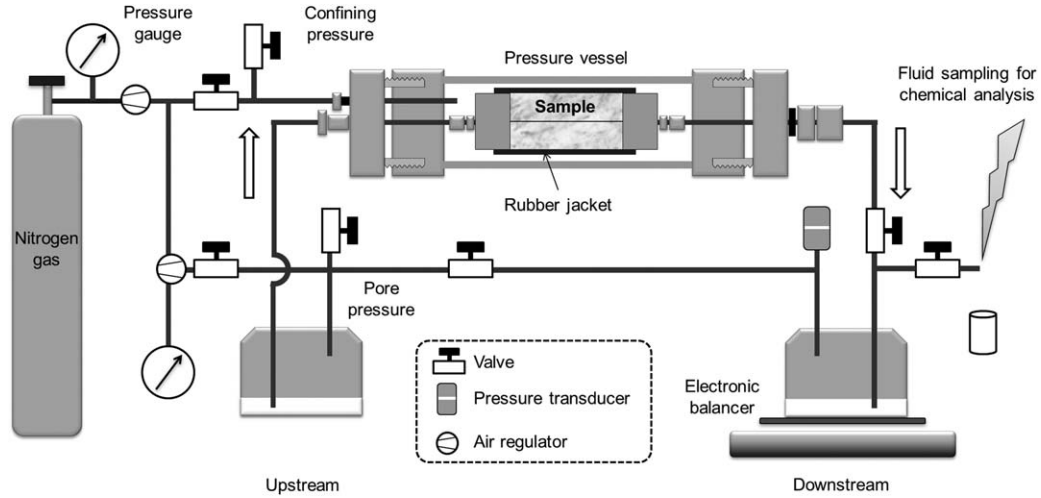
Figure 2. Schematic illustration of experimental arrangement for the flow-through experiments.
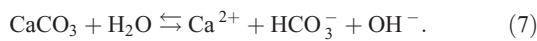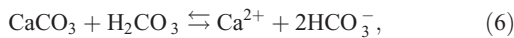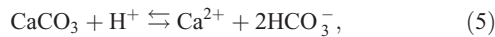
2009; *Watanabe et al.*, 2009]. The hydraulic aperture of the single fracture in the sample is evaluated as

$$e_h = \left(-\frac{12\mu LQ}{W\Delta P} \right)^{1/3}, \qquad (4)$$

[12] where e_h is hydraulic aperture [L]), Q is the flow rate [$L^3 T^{-1}$])], ΔP is the differential pressure [$MT^{-2}L^{-1}$], μ is the viscosity of the injected fluid [$ML^{-1}T^{-1}$], and L and W are, respectively, apparent length of the fracture in the directions parallel and perpendicular to the macroscopic flow direction [L].

2.3. Chemical Analysis

[13] Fluid at prescribed pH is flowed throughout the experiment and the effluent fluid sampled at suitable intervals. Dissolution of calcite advances according to the following reactions [*Wigley and Plummer*, 1976; *Plummer et al.*, 1978; *Chou et al.*, 1989]:

$$CaCO_3 + H^+ \leftrightarrows Ca^{2+} + 2HCO_3^-, \qquad (5)$$

$$CaCO_3 + H_2CO_3 \leftrightarrows Ca^{2+} + 2HCO_3^-, \qquad (6)$$

$$CaCO_3 + H_2O \leftrightarrows Ca^{2+} + HCO_3^- + OH^-. \qquad (7)$$

[14] The dominant reaction within these three reactions depends on the pH of the flowing fluid.

Table 2. Characteristics of Flowing Fluid Used in the Experiments

Number of Flowing Fluid	Concentration of Ammonium Chloride (kg/m^3)	Theoretical Value of pH	Measured Value of pH
1	9.31	5.00	5.20
2	9.31×10^{-2}	6.00	5.61
3	5.89×10^{-2}	6.10	5.82
4	2.34×10^{-2}	6.30	6.06
5	9.31×10^{-3}	6.50	6.25
6	0 (distilled water)	7.00	6.54

[15] In these reactions, the principal component in the solution is Ca, derived from dissolution from both contacting and noncontacting asperities of the fracture surface. Effluent concentration of the calcium is obtained by assaying the samples with inductively coupled plasma emission spectrometry (ICP-AES via Perkin-Elmer Optima 5300DV), and includes an estimated relative error of ±5%. The total mass transfer rate of calcite from both contacting and noncontacting asperities of the fracture surface is determined from the following equation [*Polak et al.*, 2003, 2004]:

$$\left(\frac{dM}{dt} \right)_{total} = \frac{W_{CaCO_3}}{W_{Ca}} \cdot Q \cdot C_{Ca}, \qquad (8)$$

[16] where $\left(\frac{dM}{dt} \right)_{total}$ is the total mass transfer rate [MT^{-1}], W_{CaCO3} and W_{Ca} are, respectively, molar weight of calcite and calcium [ML^{-3}], Q is the flow rate [L^3T^{-1}], and C_{Ca} is effluent Ca concentration [ML^{-3}]. Note that the corresponding uncertainty in the estimate of the mass transfer rate is also ±5%. Total mass fluxes are defined by normalizing the total mass transfer rates with the corresponding surface areas (product of diameter and length of core) of fractures shown in Table 1. The real reactive surface areas are larger than these nominal surface areas but will be correlated with the nominal magnitudes. In the present flow-through experiments the pH of the effluent is not measured.

3. Experimental Results and Analyses

[17] We examine the evolution of permeability within the fracture due to the redistribution of mineral mass within the fracture. This is due to dissolution and reprecipitation [*Yasuhara et al.*, 2006a, 2006b; *Detwiler and Rajaram*, 2007] and also due to pressure solution [*Rutter*, 1976; *Stephenson et al.*, 1992; *Revil*, 1999; *Taron and Elsworth*, 2010]. These effects operate in different polarities: free-face dissolution increases net aperture and permeability [*Polak et al.*, 2004; *Yasuhara et al.*, 2006b] while reprecipitation and pressure dissolution at the contacting asperities decrease the aperture and permeability [*Yasuhara et al.*, 2006b; *Taron and Elsworth*, 2010]. These experiments are

completed at sufficiently high flow rates that the flowing fluid remains chemically undersaturated and reprecipitation is not favored. These dynamic processes are constrained from concurrent measurements of instantaneous fluid flow rates (constraining permeability) and calcium ion concentrations in the effluent fluid (constraining change in volume of void within fracture). These measurements are independent but complementary in that they allow each constraint of changes in hydraulic aperture over time, which in turn contributes to permeability evolution.

[18] The extensive suite of experiments map regimes of permeability change including regimes of both increasing and decreasing fracture permeability for the controlled parameters of reactivity (pH) of influent fluid and ambient confining stress.

3.1. Evolution in Fracture Aperture

[19] The present study uses four limestone samples (TD01, TD02, TD03, and TD04) for multiple repeats of experiments after regrinding. The sequence of experimental conditions is documented in Table 3 defining the specific surface dimensions for each experiment. Note that we report the experimental results in terms of the theoretical values. This is because the measured pH values have dispersion for the fluid with an arbitrary concentration of ammonium chloride. We do not independently measure the dispersion in the present study.

[20] The evolution of measured flow rate for the experiments performed in this study are shown in Figure 3, and the corresponding changes in hydraulic aperture are depicted in Figure 4. The hydraulic aperture is evaluated from the recorded flow rates and prescribed differential pressure via the cubic law (i.e., equation (4)). To isolate the influence of influent pH, we first show the evolutions of flow rate and calculated hydraulic aperture at invariant confining stresses of 3, 5, and 10 MPa. By using the flow rates and hydraulic apertures provided in Figures 3 and 4, the residence time of fluid within the fracture is calculated to be of
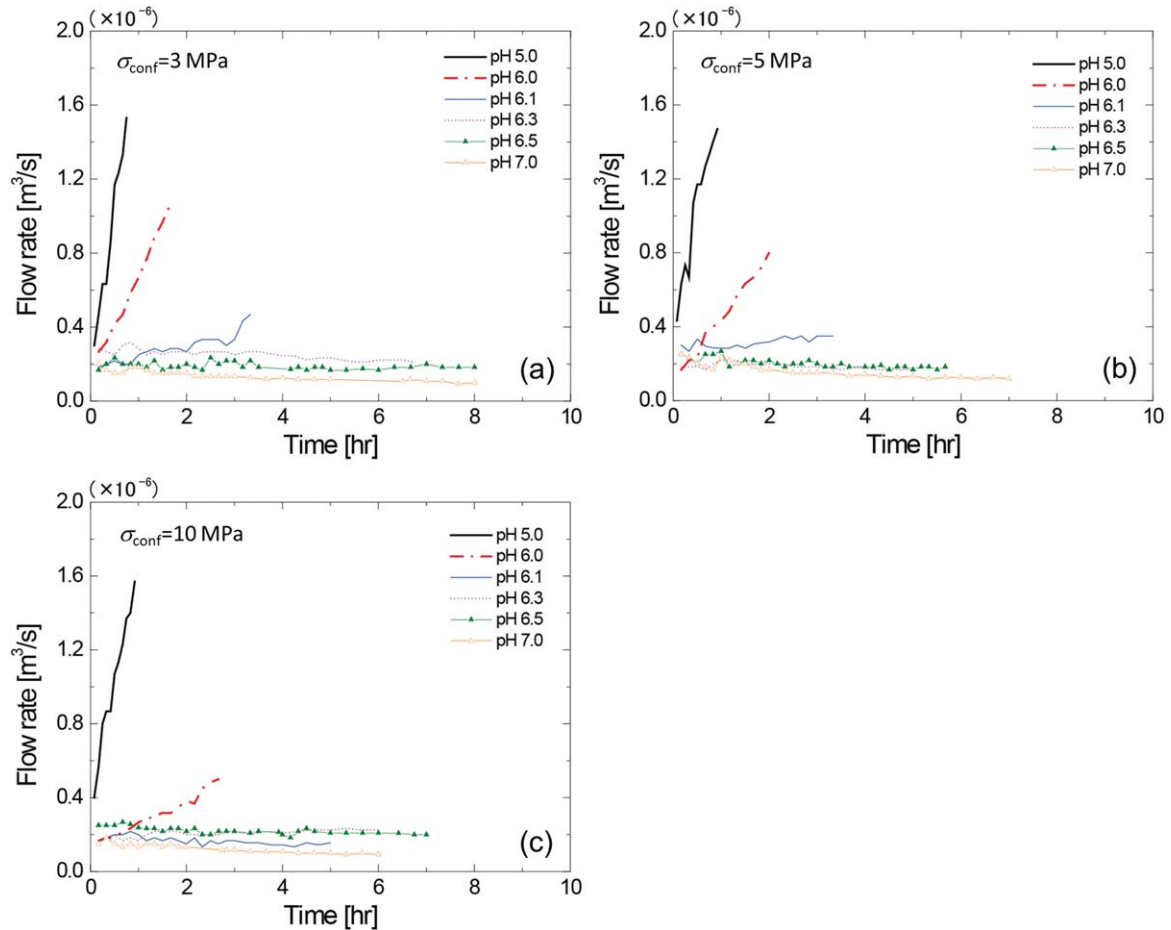
the order of a few tenths of a second. In this range of confining stresses, the hydraulic aperture increases monotonically when the influent pH is less than 6.1 and decreases when the influent pH is greater than 6.5. The switch from aperture gaping to closing corresponds to a reactivity of influent fluid in the transitional range pH $\sim$6.1–6.5.

[21] For the experiments where the influent pH is less than 6.1, monotonic increase in the fracture aperture may be attributed to the relative dominance of free-face dissolution over the shortening of the fracture bridging asperities. Conversely, for the experiments where the influent pH is more than 6.5, reduction in fracture aperture is attributed to the relative dominance of dissolution at the contacting asperities of the fractures. Moreover, for the experiments in the transitional regime ($6.1 < pH < 6.5$), the invariant flow rate and related hydraulic aperture represent a balance between the two mechanisms of free-face dissolution and shortening of the bridging asperities. Importantly, this balance does not necessarily represent a balance in the masses removed by each mechanism, as these mass fluxes must scale with the ratios of the free-face and asperity contact areas [*Yasuhara et al.*, 2006a, 2006b; *Elsworth and Yasuhara*, 2006].

[22] Subsequently, the influence of confining stress on the time-evolving hydraulic aperture is examined in Figure 5, where fluid flows at invariant influent pH value (theoretically adjusted) of 5.0, 6.0, 6.1, 6.3, 6.5, and 7.0. The time-evolving hydraulic aperture (proxy for permeability evolution) is approximated by a straight line, and the slope of this line (change in hydraulic aperture over time) is the rate of aperture change (positive for aperture gaping). Calculated rates of aperture change from Figure 5 are shown in Table 3 for various combinations of influent pH and confining stress. The rate of aperture closing is less than 1.04 μm/hr at confining stresses of 3–10 MPa and is relatively small compared to the rate of aperture gaping (see Table 3). Despite this small rate, the measurement is robust as it is recovered from a calculated change in permeability where the respective flow rate is accumulated over a period of

Table 3. Summary of Experimental Observation for Various Combinations of Confining Stress and Influent pH

Confining Stress (MPa)	Theoretical pH Value of Flowing Fluid	Differential Pressure (kPa)	Sample Number	Total Volume of Flowing Fluid (m^3)	Change in Hydraulic Aperture Over Time (μm/h)	Mass Flux (kg m^{-2} s^{-1})
3.0	5.0	100	TD 04	2.5×10^{-3}	40.77	5.65×10^{-5}
	6.0	100	TD 03	3.8×10^{-3}	14.85	6.40×10^{-6}
	6.1	100	TD 01	3.5×10^{-3}	3.28	4.10×10^{-6}
	6.3	100	TD 03	6.0×10^{-3}	−0.57	1.12×10^{-6}
	6.5	100	TD 01	5.4×10^{-3}	−0.20	1.12×10^{-6}
	7.0	100	TD 04	3.7×10^{-3}	−0.71	5.58×10^{-7}
5.0	5.0	100	TD 04	3.4×10^{-3}	29.17	5.44×10^{-5}
	6.0	100	TD 04	3.4×10^{-3}	11.66	7.98×10^{-6}
	6.1	100	TD 01	3.8×10^{-3}	0.98	3.11×10^{-6}
	6.3	100	TD 03	3.3×10^{-3}	−0.41	1.52×10^{-6}
	6.5	100	TD 01	4.1×10^{-3}	−0.70	8.20×10^{-7}
	7.0	100	TD 04	3.8×10^{-3}	−1.04	5.87×10^{-7}
10.0	5.0	100	TD 02	3.4×10^{-3}	28.50	5.80×10^{-5}
	6.0	300	TD 02	3.0×10^{-3}	4.16	4.12×10^{-6}
	6.1	300	TD 02	3.0×10^{-3}	−0.51	1.90×10^{-6}
	6.3	200	TD 02	4.5×10^{-3}	0.31	9.41×10^{-7}
	6.5	200	TD 02	5.5×10^{-3}	−0.32	5.66×10^{-7}
	7.0	200	TD 04	2.6×10^{-3}	−0.94	5.58×10^{-7}

Figure 3. Evolution of flow rate during flow-through experiments at theoretical pH of the influent fluid of 5–7 and at confining stresses of (a) 3 MPa, (b) 5 MPa, and (c) 10 MPa.

20 min. This accumulated flux is then weighed with differences of the order of ~10 g identifying the change in mass flow rate and therefore an unequivocal and measurable decrease in permeability (and related aperture).

[23] The rates of aperture change are shown in Figure 6, indicating that the permeability increases monotonically when the influent pH is less than 6.1 and decreases when the influent pH is greater than 6.5. This map shows that the rate of aperture change decreases with an increase in influent pH for invariant confining stresses of 3, 5, and 10 MPa. This map of permeability evolution includes a transitional regime linking aperture gaping to aperture closing ($6.1 < pH < 6.5$). Figure 6 also suggests that the rate of aperture change (gaping) decreases with an increase in the confining stress when the influent pH is 5.0, 6.0, or 6.1. Conversely, a clear trend for the rate of aperture change (closing) with an increase in confining stress cannot be observed when the influent pH is 6.3, 6.5, and 7.0.

3.2. Surface Dissolution

[24] The effluent concentration of calcium is monitored throughout the flow-through experiments with no particulate matter apparent in the effluent fluid. Measured concentrations are always lower than equilibrium calcium solubilities due to the short residence time of the fluid within the fracture (about a few 10ths of a second). This implies that the effect of precipitation on permeability evolution can be ignored for these particular experimental conditions. Figure 7 shows the change in the mass flux of calcite with elapsed time for the experiments at invariant confining stresses of 3, 5, and 10 MPa. The change in mass flux of calcite with respect to time is small. Average magnitudes of the mass flux of calcite over the test duration are calculated for various combinations of the confining stress and influent pH (Table 3) and are included in Figure 8.

[25] Figure 8 shows that the mass flux of calcite from the fracture surface, which is calculated by using the measured Ca concentration of effluent, is clearly pH dependent. At confining stresses of 3–10 MPa, a decrease in the pH of the influent fluid enhances the mass transfer rate. A notable finding is that a significant change in the mass flux is observed for a theoretical pH value in the range 5.0–6.0. *Chou et al*. [1989] have reported that the net rate of calcite dissolution changed dramatically over almost the same pH region of contacting fluid (5.0–6.0), and this characteristic of calcite dissolution conforms to our experimental results.

[26] Subsequently, the dependency of calcite mass flux on confining stress is examined for invariant influent pH values of 5.0, 6.0, 6.1, 6.3, 6.5, and 7.0. No clear trend for calcite mass flux with an increase in confining stress can be observed at any influent pH values. At confining stresses between 3 and 10 MPa the mass flux of calcite assumes
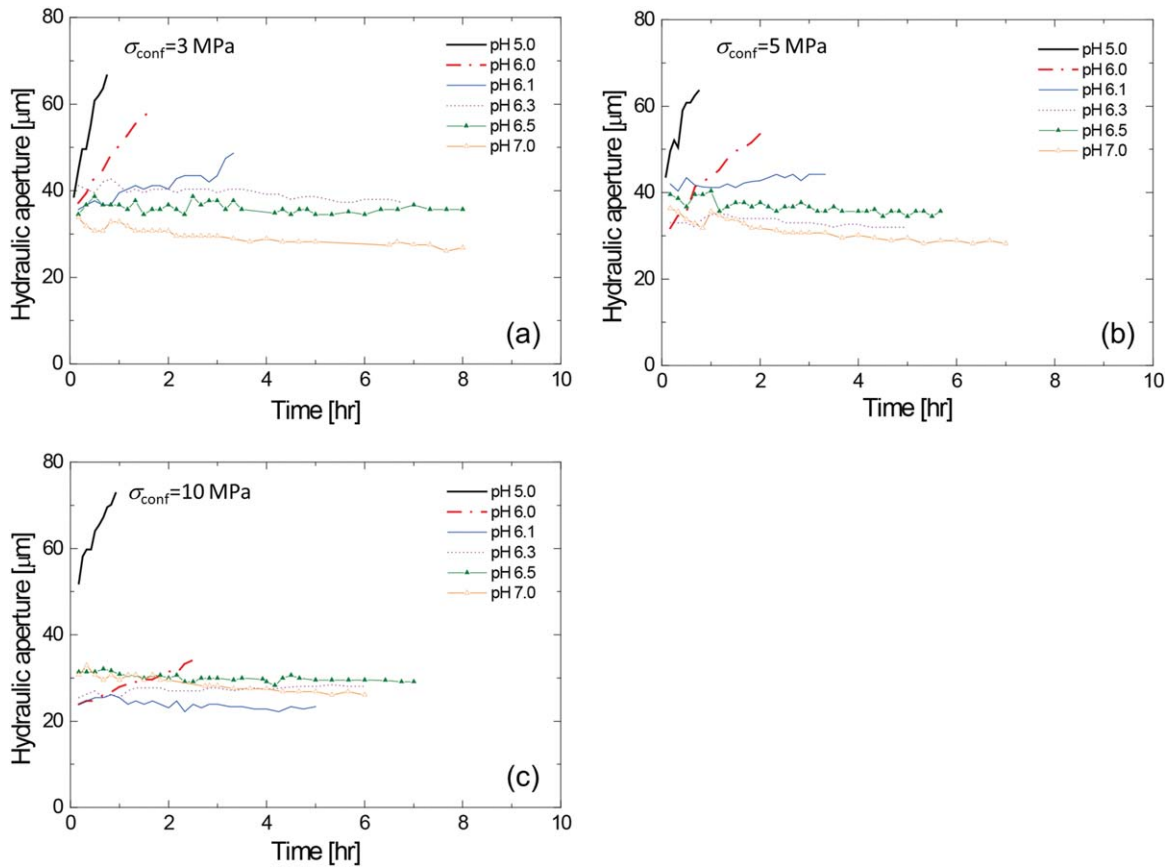
Figure 4. Evolution of permeability-derived hydraulic aperture of the fractures in carbonate during flow-through experiments at theoretical pH of the influent fluid of 5–7 and at confining stresses of (a) 3 MPa, (b) 5 MPa, and (c) 10 MPa.

almost the same value for a particular influent pH, and any small difference in the mass flux for a particular influent pH is due to the difference in original void distribution on the face of the fracture surface (see Figure 1).

4. Interpretation by Lumped Parameter Model

[27] Permeability evolution of these carbonate fractures is evaluated for various combinations of confining stress (3, 5, and 10 MPa) and influent pH (5.0, 6.0, 6.1, 6.3, 6.5, and 7.0). Experimental results suggest the following: (1) up to a confining stress of 10 MPa, hydraulic aperture (permeability) increases monotonically when the influent pH is less than ~6.1 and then decreases when the influent pH is greater than ~6.5 and (2) the transitional pH regime of invariant hydraulic aperture is between 6.1 and 6.5.

[28] In examining our experimental results, it should be noted that the dissolution rate constant for calcite is relatively high (e.g., 2.51×10^{-9} mol m^{-2} s^{-1} for quartz sand at 150°C, and 1.25×10^{-6} mol m^{-2} s^{-1} for calcite at 20°C (neutral pH condition)) [Plummer et al., 1978; Chou et al., 1989; Dove and Crerar, 1990]. This means that the effect of pressure solution for carbonate fractures can be observed at room temperature. Additionally, in our experiments, no particulate matter is observed in the effluent fluid, which suggests that a concept of particle-detachment might be inappropriate as an explanation for aperture reduction.

Therefore, one of the most likely mechanisms is pressure solution as observed elsewhere [Polak et al., 2004; Elsworth and Yasuhara, 2006; Yasuhara et al., 2006b].

[29] A monotonic increase in fracture aperture (and corresponding permeability) when the influent pH is less than 6.1 can be explained by the relative dominance of free-face dissolution at noncontacting asperities (fracture void) over pressure solution at contacting asperities [Polak et al., 2004; Yasuhara et al., 2006b]. In contrast to this, monotonic reduction in hydraulic aperture when the influent pH is more than 6.5 can be explained by the relative dominance of pressure solution at contacting asperities [Yasuhara et al., 2004; Taron and Elsworth, 2010]. As a result, we employ a lumped-parameter model to interpret the dissolution-dominant evolution of fracture permeability in the following. In our model, permeability evolution is controlled by the competition between two mechanisms: pressure solution at contacting asperities and dissolution at the free-face surfaces of fractures [Elsworth and Yasuhara, 2006; Yasuhara et al., 2006a, 2006b]. The details of this lumped parameter model are as follows.

4.1. Evolution of Hydraulic Aperture (Gaping or Closing)

[30] A representative elemental volume (REV) of the fracture is shown in Figure 9. The pore space is filled with the permeant and defined by local hydraulic aperture, e_h. It
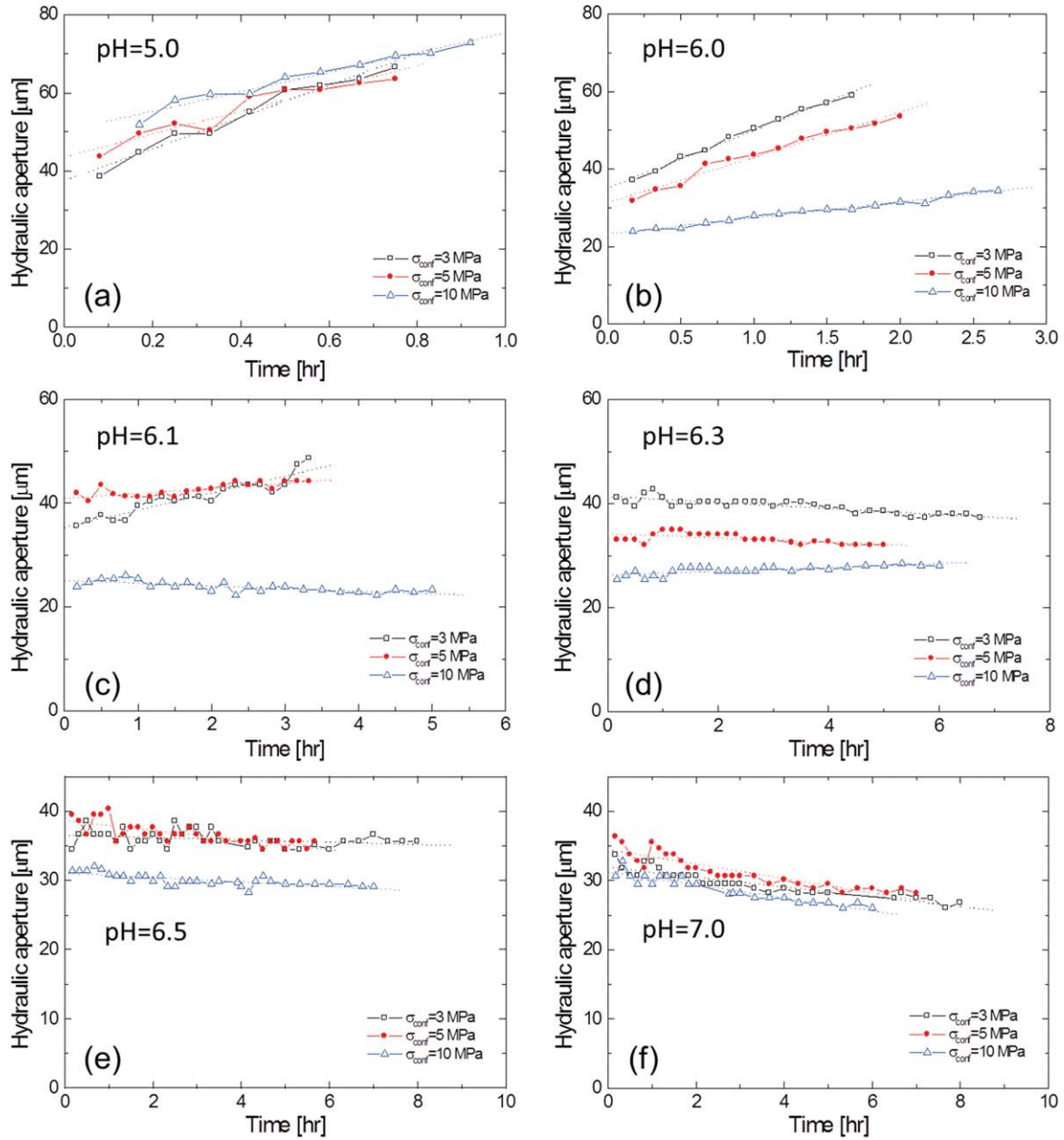
Figure 5. Evolution of permeability-derived hydraulic aperture of fractures in carbonate during flow-through experiments at confining stresses from 3 to 10 MPa, where the theoretical pH of the influent fluid is (a) 5.0, (b) 6.0, (c) 6.1, (d) 6.3, (e) 6.5, and (f) 7.0.

is generally accepted that contacting asperities are coated with water films. The thickness of these water films is assumed to be of the order of nanometers [*Heidug*, 1995; *Tokunaga*, 2011; *Abe et al.*, 2012] and is much smaller than the apertures at noncontacting asperities. In the present model, the permeant is in contact with both upper and lower free-face surfaces of the fracture. The time-dependent change in contact area is not measured in our experiments, but experimental results indicate that the time-evolving hydraulic aperture is approximated by a straight line during the test duration (see Figure 5). This fact supports the time-independent contact area, which means that contact area is expressed as a function of confining stress only.

[31] Considering a single contacting asperity, the mass transfer rate derived from pressure solution at contacting asperities, $\frac{dM_{diss}^{ps}}{dt}$, is given as [*Rutter*, 1976; *Yasuhara et al.*, 2004]

$$\frac{dM_{diss}^{ps}}{dt} = \frac{3V_m^2 \cdot \rho_g \cdot A_{local} \cdot R_c}{RT}\left(\frac{\sigma_{conf}}{R_c} - \sigma_{crit}\right) \cdot k_1, \qquad (9)$$

[32] where V_m is molar volume of the solid (3.69×10^{-5} m^{3}mol^{-1} for calcite), σ_{conf} is confining stress, $_1$ is the dissolution rate constant of the solid at the contacting asperities, ρ_g is the grain density (2710 kg m^{-3} for calcite), A_{local} is the fracture area within the representative volume, R_c is the
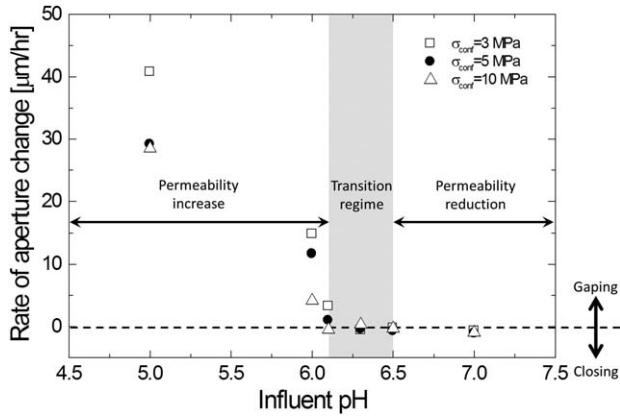
Figure 6. The rate of aperture change recovered from the evolution in fracture permeability for various combinations of influent pH and confining stress.

contact-area ratio, R is the gas constant, T is the absolute temperature of the system (298 K in our study), and σ_{crit} is the critical stress [*Yasuhara et al.*, 2004; *Taron and Elsworth*, 2010]. This critical stress defines a stress state where the compaction at contacting asperities will effectively halt. This stress is determined by considering the energy

balance under applied stress and temperature conditions, given as (*Revil* [1999], modified from *Stephenson et al.* [1992])

$$\sigma_{crit} = \frac{E_m\left(1 - \frac{T}{T_m}\right)}{4V_m},\qquad(10)$$

[33] where E_m and T_m are the heat and temperature of fusion, respectively ($E_m = 36$ kJ mol^{-1}, $T_m = 1603$ K for calcite). The calculated critical stress ($\sim$200 MPa) is modified after *Yasuhara et al.* [2006b] so that a large decrease in hydraulic aperture ($\sim$8 μm) can be predicted. We need more data to support this modification, as we have no such an independent observation in this work.

[34] The mass transfer rate derived from dissolution at the free-fracture surfaces,$\frac{dM_{diss}^{ff}}{dt}$, is given by

$$\frac{dM_{diss}^{ff}}{dt} = 2 \cdot k_2 \cdot A_{local} \cdot (1 - R_c) \cdot \rho_g \cdot V_m\left(1 - \frac{C_{pore}}{C_{eq}}\right),\qquad(11)$$

[35] where k_2 is the dissolution rate constant of the solid at the fracture free face, C_{pore} is the solute concentration in the pore space, and C_{eq} is the equilibrium solubility of the dissolved mineral [*Palmer*, 1991; *Yasuhara et al.*, 2004,
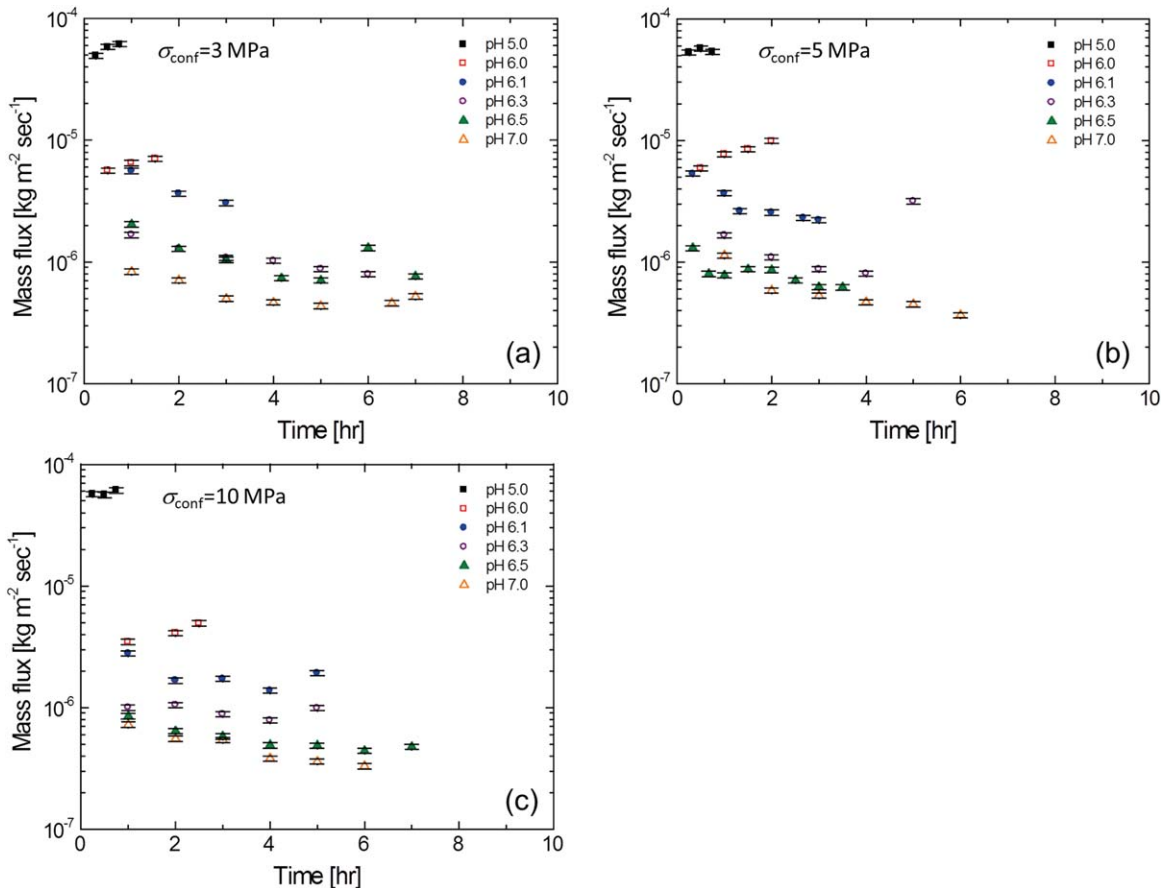
Figure 7. Change in the mass flux of calcite during the flow-through experiment with the theoretical pH of the influent fluid from 5.0 to −7.0 at confining stress of (a) 3 MPa, (b) 5 MPa, and (c) 10 MPa. Error bars are created for a relative error of 5%.
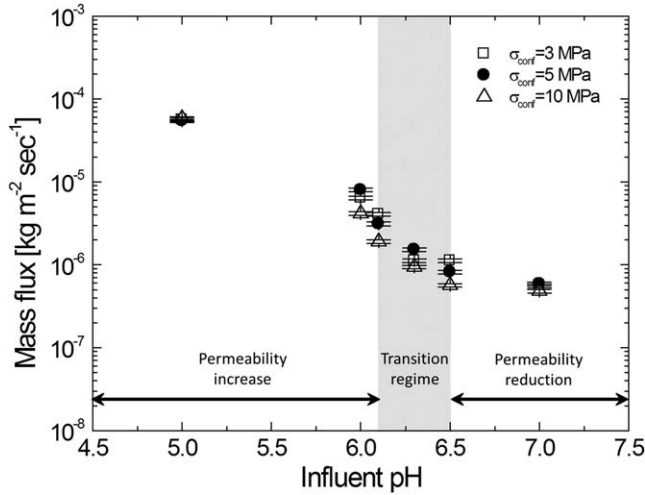
Figure 8. Average values for the mass flux of calcite over the test duration for various combinations of theoretical pH of the influent fluid and confining stress. Error bars are created for a relative error of 5%.

2006a, 2006b]. Note that the factor of 2 in equation (11) is derived from free-face dissolution for both upper and lower fracture surfaces in Figure 9. As described earlier, measured magnitudes of C_{pore} are much lower than those of C_{eq} in the present study, allowing C_{pore}/C_{eq} be approximated as zero.

[36] Throughout the fluid-flow experiment, fresh influent fluid of specified pH is constantly supplied to the pore space with fluid (i.e., water film) considered stagnant at the contacting asperities of the fracture. This is because the thickness of the water film is much smaller than that of apertures at noncontacting asperities (Figure 9), and fluid would flow around contacting asperities. Such a circulating flow within a fracture is also suggested by *Watanabe et al.* [2009]. For minimally reactive materials such as quartz, the dissolution rate constant shows an Arrhenius-type dependence on temperature [*Dove and Crerar*, 1990; *Yasuhara et al.*, 2004], and the pH of the contacting fluid has little or no influence on the dissolution rate constant. As a result, the dissolution rate constant at the contacting asperities (k_1) is generally assumed to be the same as that at the free-fracture surfaces (k_2), although some degree of discrepancy between experiments and predictions under this assumption might be confirmed [*Noort and Spiers*, 2009]. In contrast, for highly reactive materials such as carbonate, not only temperature but also the pH of the contacting fluid has a significant influence on the net dissolution constant of the materials [*Plummer et al.*, 1978; *Chou et al.*, 1989]. Therefore, it is of critical importance to incorporate the influence of pH at both contacting asperities and at the free-fracture surfaces. In the case of our lumped parameter model, hydronium ions are consumed for carbonate dissolution by the stagnant water films due to the high dissolution rate of calcite, resulting in a pH increase at the contacting asperities. When the pH of the influent fluid is lower than the pH at the contacting asperities, the hydronium ions would certainly diffuse along the water films. However, these hydronium ions are immediately consumed due to the pH decrease (or increase in dissolution rate) at the contacting asperities. Considering these mechanisms, the pH at the contacting asperities is expected to be equal to or greater than the influent pH. Consequently, k_1 is equal to k_2 in the former case, while k_1 is lower than k_2 in the latter case. These two conjectures are explored in the subsequent section, since our experimental results cannot constrain the pH value at contacting asperities.
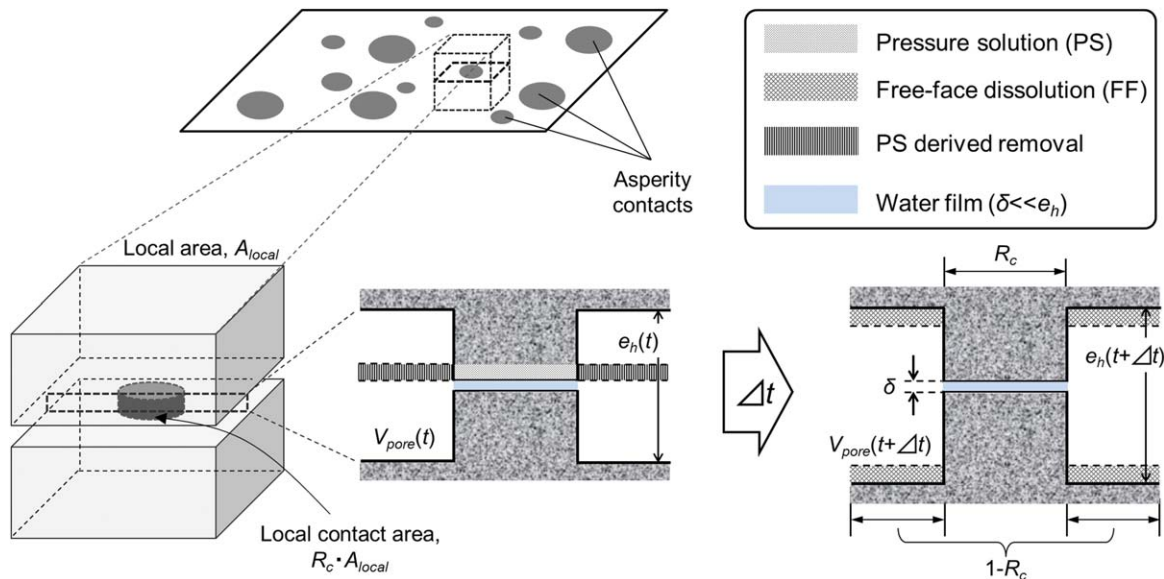
Figure 9. Schematic illustration of the REV in the immediate vicinity of the fracture. Contacting asperities are assumed to be coated with water film of some nanometers. Pressure solution at the contacting asperities and dissolution at the free surfaces of the fracture each contribute to a change in fracture aperture.

[37] At a given time, t, the pore volume within the REV, $V_{\text{pore}}(t)$, is given by

$$V_{\text{pore}}(t) = A_{\text{local}} \cdot e_h(t), \tag{12}$$

[38] where $e_h(t)$ is the hydraulic aperture of the fracture. The pore volume evolves due to the effects of both pressure solution at the contacting asperities (reducing volume) and a result of free-face dissolution (increasing volume). As represented in Figure 9, the pore volume after the time step Δt, $V_{\text{pore}}(t+\Delta t)$, is given by

$$V_{\text{pore}}(t + \Delta t) = V_{\text{pore}}(t) - \frac{dM_{\text{diss}}^{\text{ps}}}{dt} \cdot \frac{1}{\rho_g} \cdot \Delta t \cdot \frac{1 - R_c}{R_c} + \frac{dM_{\text{diss}}^{\text{ff}}}{dt}$$
$$\cdot \frac{1}{\rho_g} \cdot \Delta t$$
$$= A_{\text{local}} \cdot e_h(t + \Delta t), \tag{13}$$

[39] where $e_h(t+\Delta t)$ is the hydraulic aperture of the fracture after a time step Δt. The rate of change in hydraulic aperture (gaping or closing), de_h/dt, is defined as

$$\frac{de_h}{dt} = \frac{e_h(t + \Delta t) - e_h(t)}{\Delta t}$$
$$= \frac{1}{A_{\text{local}} \cdot \rho_g} \cdot \left(-\frac{dM_{\text{diss}}^{\text{ps}}}{dt} \cdot \frac{1 - R_c}{R_c} + \frac{dM_{\text{diss}}^{\text{ff}}}{dt} \right). \tag{14}$$

[40] Substituting equations (9) and (11) into equation (14) enables de_h/dt to be rearranged to yield

$$\frac{de_h}{dt} = -\frac{3V_m^2}{RT} \cdot (1 - R_c) \cdot \left(\frac{\sigma_{\text{conf}}}{R_c} - \sigma_{\text{crif}} \right) \cdot k_1 + 2 \cdot (1 - R_c) \cdot V_m \cdot k_2 \tag{15}$$

[41] This represents the rate of change of the fracture aperture within the REV due to the dual action of free-face dissolution and pressure solution. Additionally, the mass transfer rate from the entire fracture surface comprises components from both pressure solution $\left(\frac{dM_{\text{diss}}^{\text{ps}}}{dt} \right)_{\text{total}}$ and free-face dissolution $\left(\frac{dM_{\text{diss}}^{\text{ff}}}{dt} \right)_{\text{total}}$, and is defined as

$$\left(\frac{dM}{dt} \right)_{\text{total}} = \left(\frac{dM_{\text{diss}}^{\text{ps}}}{dt} \right)_{\text{total}} + \left(\frac{dM_{\text{diss}}^{\text{ff}}}{dt} \right)_{\text{total}}$$
$$\cong \frac{3V_m^2 \cdot \rho_g \cdot A_{\text{total}} \cdot R_c}{RT} \left(\frac{\sigma_{\text{conf}}}{R_c} - \sigma_{\text{cirt}} \right) \cdot k_1$$
$$+ 2 \cdot k_2 \cdot A_{\text{total}} \cdot (1 - R_c) \cdot \rho_g \cdot V_m, \tag{16}$$

[42] where A_{total} is the total area of the fracture surface. The corresponding total mass flux is defined by normalizing the total mass transfer rate with the total surface area of the fracture, A_{total}.

4.2. Controlling Parameters

[43] This model is applied to quantify the permeability evolution in fractures in carbonate observed in flow-through experiments at constant temperature ($\sim$298 K). The rate of change of the hydraulic aperture and mass transfer rate are evaluated by equations (15) and (16), respectively. However, parameters of dissolution rate constant (k_1, k_2) have not been

directly determined as it is difficult to constrain an accurate value of contact-area ratio (R_c).

[44] The mass of calcite removed is the primary component contributing to the observed change in hydraulic aperture. In the present experiments, six different fluids with various pH values are used as the flowing fluid, and it has been widely recognized that the pH of the contacting fluid has an influence on the dissolution rate of calcite. The net rate of calcite dissolution, r, is well known from the Plummer-Wigley-Parkhurst (PWP) equation [Plummer et al., 1978]:

$$r = k_{+,1}(a_{\text{H}^+}), k_{+,2}(a_{\text{H}_2\text{CO}}), k_{+,3}(a_{\text{H}_2\text{O}}) - k_-(a_{\text{Ca}^{2+}})(a_{\text{HCO}_3}), \tag{17}$$

[45] where $k_{+,1}$, $k_{+,2}$, $k_{+,3}$ are first-order dissolution rate constants dependent on temperature, k_- is the precipitation rate constant dependent on temperature and partial pressure of carbon dioxide (p_{CO2}). a_i represents the activity for the component of i. The first two terms in this equation are functions of the bulk fluid activity of H$^+$ and the p_{CO2}, respectively. The dissolution rate constants ($k_{+,1}$, $k_{+,2}$, $k_{+,3}$, and k_-) are reevaluated at room temperature (298 K) [Chou et al., 1989], and the net rate of calcite dissolution, r, is obtained for various pH conditions. Here, p_{CO2} is approximately equal to the partial pressure of carbon dioxide in the atmosphere ($10^{-3.5}$ atm) in the present experiments. The relationship between pH value of the contacting fluid and net rate of calcite dissolution is plotted in Figure 10 with the values of net dissolution rate at specific pH conditions in the experiments also summarized in Table 4. The dissolution rate constant at the free-fracture surface, k_2, is set equivalent to the values shown in Table 4 for each pH condition.

[46] Then, the pH value at the contacting asperities is examined. When the pH at the contacting asperities is the same as the influent pH, equation (14) can be rewritten as

$$\frac{de_h}{dt} = \left\{ 2V_m - \frac{3V_m^2}{RT} \left(\frac{\sigma_{\text{conf}}}{R_c} - \sigma_{\text{crit}} \right) \right\} \cdot (1 - R_c) \cdot k_1$$
$$= \lambda(\sigma_{\text{conf}}, R_c) \cdot (1 - R_c) \cdot k_1. \tag{18}$$
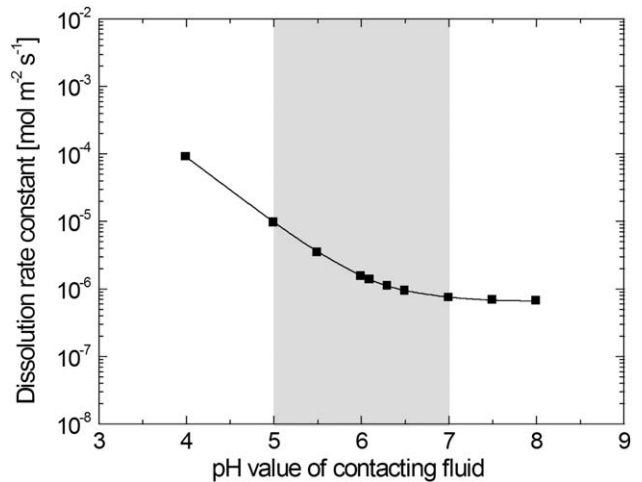
Figure 10. Log rate of calcite dissolution as a function of fluid pH at 298 K. These values are calculated based on Chou et al. [1989] by using PWP equation.

Table 4. Net Rate of Calcite Dissolution for Different pH Values (Based on *Chou et al.* [1989])

Theoretical Value of pH	Net Rate of Calcite Dissolution (mol m^{-2} s^{-1})
5.0	9.55×10^{-6}
6.0	1.54×10^{-6}
6.1	1.36×10^{-6}
6.3	1.10×10^{-6}
6.5	9.32×10^{-7}
7.0 (distilled water)	7.39×10^{-7}

[47] The magnitude of the constant $\lambda(\sigma_{conf}, R_c)$ in this equation is uniquely determined by specifying confining stress. The net rate of calcite dissolution decreases with an increase in pH as shown in Figure 10. In order to reproduce the experimental results in that the rate of change in hydraulic aperture decreases with an increase in fluid pH, the parameter $\lambda(\sigma_{conf}, R_c)$ must be positive in equation (18). However, experimental results further include the transition between aperture gaping and closing at arbitrary confining stress, and this characteristic cannot be reproduced by equation (18). Because of this observation, it is not reasonable to assume that the pH at the contacting asperities is equivalent to the influent pH—therefore, the pH at the contacting asperities is assumed higher than the influent pH in the following analysis.

[48] One limitation of our current experimental measurements is that it is not possible to determine the exact pH value at the contacting asperities. Thus, we focus on the observation that the change in net rate of calcite dissolution is not significant when the pH value of the contacting fluid is more than ~6.0 (up to ~8.0) [*Plummer et al.*, 1978; *Chou et al.*, 1989]. Considering the relatively high reactivity of calcite, it is not surprising that the pH at contacting asperities would be more than ~6.0. Therefore, representing the pH at contacting asperities as ~7.0 (near neutral) is one practical way to constrain response. This means that the dissolution rate constant, k_1, is set equivalent to 7.39×10^{-7} mol/m^2/sec in the present study (see Table 4).

[49] The dissolution rate constant for both contacting asperities (k_1) and free-fracture surface (k_2) are now determined, and the only remaining unknown parameter is the contact-area ratio (R_c) in equations (15) and (16). There is no additional information to constrain the value of R_c. Therefore, for the different confining stress conditions (3, 5, and 10 MPa), the contact-area ratio, R_c, is determined as a fitting parameter. By adjusting R_c, the specific pH corresponding to the transit from fracture gaping to closing varies, while no drastic change is observed in the mass flux, which is obtained by normalizing equation (16) with A_{total}, for the specified combination of influent pH and confining stress (Figure 11). As a result, R_c is selected for respective confining stress conditions so that the transition pH in the present model may be matched with the transitional pH defined from the experimental observations. The match with experiments is the best at a contact-area ratio of 3.3% ($R_c = 0.033$), 5.5% ($R_c = 0.055$), and 11.8% ($R_c = 0.118$) when the confining stress is 3, 5, and 10 MPa, respectively. This suggests that fracture contact area increases with increased stress—a reasonable, but unmeasured, expectation.
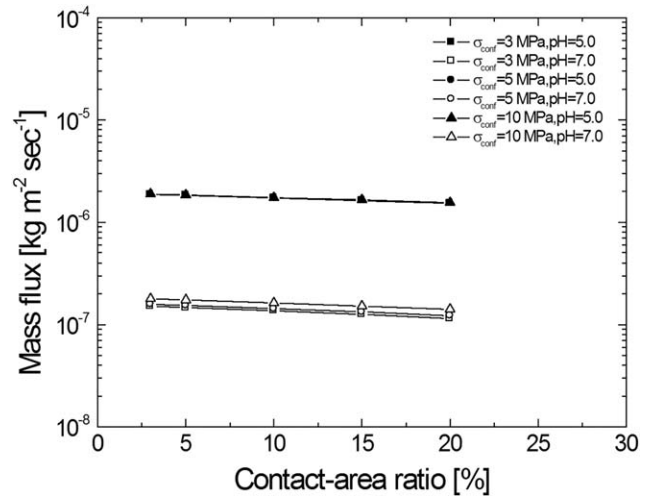
Figure 11. Change in mass flux of calcite, which is calculated by the present lumped-parameter model, on the contact-area ratio for various combination of confining stress and influent pH.

4.3. Predicted Versus Observed Behavior

[50] By substituting these selected parameters into equations (15) and (16), the rate of aperture change and total mass transfer rate from both pressure solution and free-face dissolution is calculated for various combinations of influent pH and confining stress. For these selected parameters, a comparison of results of total mass flux (derived by normalizing the mass transfer rate with the fracture surface area) and rate of aperture change between experiments and model are shown in Figures 12 and 13 with thin lines, respectively. For this consistent suite of parameters, the model is capable of following the transit from aperture gaping to aperture closing at the specific influent pH for various confining stress conditions. However, regarding absolute amounts for both the rate of aperture change and total mass flux, the predicted values are approximately 10 times smaller than the measured values. As shown in Figure 11, for a specified combination of influent pH and confining stress, the total mass flux is nearly invariant with the change in contact area. This means that changing the contact-area ratio is not the solution to these discrepancies in the present model.

[51] In order to closely match the rate of aperture change and total mass flux in the experiments, the significant parameters of reaction rate constants for pressure solution (k_1) and free-face dissolution (k_2) in equations (15) and (16) are increased by a factor of 10. Here, we should note that the adjustment of reactive surface area does not influence the rate of aperture change in the present model (equation (15)). The reason for the adjustment of the reaction rate constants is to accommodate the diversity of properties for calcite (grain size, crystallinity, impurities, and defect density), which closely relates to the variation in the dissolution rate. The calcite evaluated in the previous study of *Chou et al.* [1989] is not the same as that in the present study, and significant uncertainty in the absolute value of calcite dissolution rate constants is reported in *Arvidson et al.* [2003]. They show that although the dependency of the
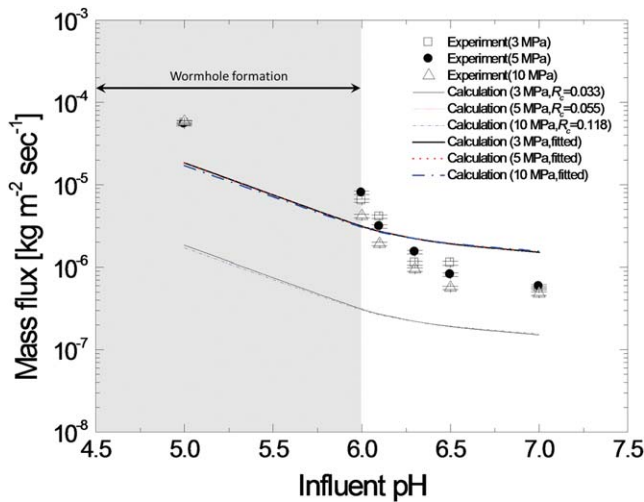
Figure 12. Comparison of the mass flux either measured experimentally or recovered from the lumped-parameter modeling for various combinations of the theoretical pH of the influent fluid and confining stress. Thin lines and bold lines represent the predictions using original parameters and modified parameters, respectively.

dissolution rate on fluid pH is consistent for results from a given laboratory, the absolute rates vary by greater than an order of magnitude. For these modified parameters of k_1 and k_2, total mass flux and the rate of aperture change are recalculated for various combinations of influent pH and confining stress, and the comparison between experiments and models are shown in Figures 12 and 13, respectively. Mass fluxes and rates of aperture change calculated with the original values of k_1 and k_2 and with the modified values are summarized in Table 5. As shown in Figures 12 and 13, absolute amounts for the rate of aperture change and
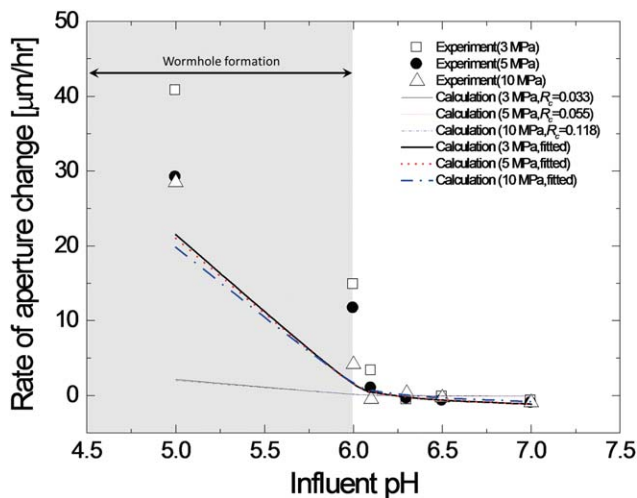
Figure 13. Comparison of the rate of aperture change (gaping or closing) recovered from experimental observations or from lumped-parameter modeling for various combinations of the theoretical pH of the influent fluid and confining stress. Thin lines and bold lines represent the predictions using original parameters and modified parameters, respectively.

mass flux match observations when using modified values of k_1 and k_2.

[52] In the present lumped-parameter model, no clear dependency of mass flux on confining stress could be observed at any influent pH values although mass flux decreases with an increase in influent pH value at any confining stress (Figure 12). These characteristics correspond to experimental observations. For the present model, mass transfer rate derived from pressure solution at contacting asperities and mass transfer rate derived from dissolution at the free-fracture surface are separately calculated (Table 5). Mass transfer rate derived from free-face dissolution clearly dominates (more than 83% of total mass flux) at confining stresses between 3 and 10 MPa. Although mass transfer rate derived from pressure solution would show a dependency on confining stress, its contribution to the total mass transfer rate is very small. Thus, the total mass transfer rate shows no stress dependency, and the resulting total mass flux is almost the same for various confining stresses. Moreover, the difference of mass flux between observations and models seems to be greater when influent pH is lower (~5), and this difference is possibly due to the fact that dissolution in the rock matrix or along the edges of the cylindrical sample occurs in our flow-thorough experiments.

[53] With respect to the rate of aperture change, a significant difference between predicted and observed values is apparent for influent pH values in the range 5.0–6.0. This discrepancy is mainly due to the fact that the formation of wormholes within the fracture [*Polak et al.*, 2004] is not considered in the present model. It is well known that fracture permeability increases abruptly with wormhole formation because the flowing fluid focuses into a preferential flow path. The present model reproduces the experimental characteristics in that the rate of aperture change decreases with an increase in the influent pH value and transits from aperture gaping to closing at any confining stress. However, no drastic dependency in the rate of aperture change on confining stress could be observed at any influent pH values (Figure 13). This characteristic is incongruous with the experimental observation particularly in that the observed rate of aperture change shows a clear reduction with an increase in confining stress for influent pH values of 5.0–6.0. Considering that the discrepancy between model and observation is clear only when the pH of the influent fluid is relatively low then the observed stress dependency of the rate of aperture change is caused principally by the formation of a wormhole. Extrapolating this observation with experimental results suggests that the ability to create wormholes decreases with an increase in the confining stress (i.e., increase in the contact-are ratio [*Nemoto et al.*, 2009; *Watanabe et al.*, 2009]).

[54] This lumped-parameter modeling provides a potential process-based explanation of permeability evolution within fractures, resulting from the combined action of stress and dissolution. This evolution in permeability is characterized by three different regimes of aperture gaping, aperture closing, and transition from aperture gaping to closing depending on the combination of confining stress and fluid pH. This characteristic is principally due to the relatively high dissolution rate of calcite and its dependence on fluid pH. In order to reproduce the transition from aperture gaping to closing, the pH (in the model) at

Table 5. Summary of Lumped-Parameter Modeling for Various Combinations of the Confining Stress and the Influent pH

Calculation Condition		Before Modification		After Modification		Ratio of Predicted Mass-Transfer Rate	
Confining Stress (MPa)	Theoretical pH Value of Flowing Fluid	Change in Hydraulic Aperture (μm/h)	Total Mass Flux (kg m^{-2} s^{-1})	Change in Hydraulic Aperture (μm/h)	Total Mass Flux (kg m^{-2} s^{-1})	Pressure Solution Derived (%)	Free-Face Dissolution Derived (%)
3.0	5.0	2.15	1.85×10^{-6}	21.47	1.85×10^{-5}	0.4	99.6
	6.0	0.09	3.06×10^{-7}	0.90	3.06×10^{-6}	2.6	97.4
	6.1	0.04	2.70×10^{-7}	0.42	2.70×10^{-6}	2.9	97.1
	6.3	−0.02	2.20×10^{-7}	−0.25	2.20×10^{-6}	3.6	96.4
	6.5	−0.07	1.88×10^{-7}	−0.67	1.88×10^{-6}	4.2	95.8
	7.0	−0.12	1.51×10^{-7}	−1.16	1.51×10^{-6}	5.2	94.8
5.0	5.0	2.10	1.82×10^{-6}	20.99	1.82×10^{-5}	0.7	99.3
	6.0	0.09	3.04×10^{-7}	0.88	3.04×10^{-6}	4.3	95.7
	6.1	0.04	2.69×10^{-7}	0.41	2.69×10^{-6}	4.9	95.1
	6.3	−0.02	2.20×10^{-7}	−0.24	2.20×10^{-6}	6.0	94.0
	6.5	−0.07	1.89×10^{-7}	−0.66	1.89×10^{-6}	6.9	93.1
	7.0	−0.11	1.53×10^{-7}	−1.14	1.53×10^{-6}	8.6	91.4
10.0	5.0	1.98	1.71×10^{-6}	19.83	1.71×10^{-5}	1.5	98.5
	6.0	0.11	2.97×10^{-7}	1.06	2.97×10^{-6}	8.6	91.4
	6.1	0.06	2.65×10^{-7}	0.63	2.65×10^{-6}	9.7	90.3
	6.3	0.00	2.19×10^{-7}	0.02	2.19×10^{-6}	11.7	88.3
	6.5	−0.04	1.90×10^{-7}	−0.37	1.90×10^{-6}	13.5	86.5
	7.0	−0.08	1.56×10^{-7}	−0.82	1.56×10^{-6}	16.4	83.6

contacting asperities must be set higher than the pH at non-contacting asperities. This enables observations to be reproduced from the model.

5. Conclusions

[55] We have described a systematic study of the interaction between mechanical and nonequilibrium chemical effects on the evolution of permeability in fractures in carbonate, where chemical effects are significant. Experimental measurements of permeability evolution in a fracture are used to constrain models for the competition between free-face dissolution and pressure solution. These effects operate in different polarities: free-face dissolution increases aperture and permeability and pressure solution at the contacting asperities decreases aperture and permeability.

[56] Experimental measurements have indicated that the permeability increases monotonically when the influent pH is less than ∼6.1 and decreases when the influent pH is greater than ∼6.5 at confining stresses to 10 MPa. The former is attributed to the relative dominance of free-face dissolution over the shortening of the fracture-bridging asperities (i.e., pressure solution), while the latter is attributed to the relative dominance of pressure solution over free-face dissolution. In the transition regime (6.1 < pH < 6.5), the invariant permeability represents a balance between these two mechanisms. Importantly, this balance does not necessarily represent a balance in the masses removed by each mechanism as closing is modulated by the relatively small contact area that props the fracture open. A series of flow-through experiments has suggested that the effect of nonequilibrium chemistry is dominant over mechanics in the evolution of permeability in carbonate fractures up to a confining stress of 10 MPa.

[57] A lumped-parameter model has been applied to constrain processes inferred from the experimental observations—that fracture permeability increases or decreases depending on the combination of confining stress and influent pH value. In order to explain the diversity of modes of permeability evolution, we have considered competition between free-face dissolution and pressure solution at contacting asperities [*Yasuhara et al.*, 2006a, 2006b]. By allowing pH at the contacting asperities to be buffered, the model potentially follows the switch from aperture gaping to aperture closing for any prescribed influent pH—as observed in the flow-through experiments. We can find a significant difference in the rate of aperture change between predicted and observed values when the influent pH is between 5.0 and 6.0. This difference is mainly due to the fact that wormhole formation [*Polak et al.*, 2004] has not been accommodated in the present model. Our results are restricted to the range before such conduits develop.

[58] In summary, we map regimes of permeability evolution for the various combinations of confining stress and fluid pH (i.e., fluid reactivity). This map illustrates a diversity of permeability evolution, and is of critical importance in understanding processes such as acidization response in carbonate reservoirs or subsurface CO_2 sequestration. The two competing roles of stress and nonequilibrium chemistry have a significant influence on long-term permeability evolution within carbonate reservoirs. Thus, the permeability of fractured carbonate reservoirs would be anticipated to decrease with time when natural fluid close to equilibrium (near neutral pH) is flowing. In contrast, permeability will increase with time when an artificially acidic fluid is introduced and flows. Acidization in carbonate reservoir is considered to be highly effective because the effect of pressure solution is very small at the corresponding pH condition of the fluid. Further detailed investigations are required to extend understanding into the evolution in fracture permeability mediated by coupled thermal, hydraulic, mechanical, and chemical processes.

References

Abe, J., N. Hirano, and N. Tsuchiya (2012), Infrared spectroscopic study of water in mesoporous silica under supercritical conditions, *J. Mater. Sci.*, *47*(23), 7971–7977, doi:10.1007/10853-012-6685-7.

Arvidson, R. S., I. E. Ertan, J. E. Amonette, and A. Luttge (2003), Variation in calcite dissolution rates: A fundamental problem? *Geochim. Cosmochim. Acta*, *67*(9), 1623–1634.

Chou, L., R. M. Garrels., and R. Wollast (1989), Comparative study of the kinetics and mechanisms of dissolution of carbonate minerals, *Chem. Geol.*, *78*, 269–282.

Detwiler, R. L., and H. Rajaram (2007), Predicting dissolution patterns in variable aperture fractures: Evaluation of an enhanced depth-averaged computational model, *Water Resour. Res.*, *43*, W04403, doi:10.1029/2006WR005147.

Detwiler, R. L., R. J. Glass, and W. L. Bourcier (2003), Experimental observation of fracture dissolution: The role of Peclet number on evolving aperture variability, *Geophys. Res. Lett.*, *30*(12), 1648, doi:10.1029/2003GL017396.

Dove, P. M., and D. A. Crerar (1990), Kinetics of quartz dissolution in electrolyte solutions using a hydrothermal mixed flow reactor, *Geochim. Cosmochim. Acta*, *54*, 955–969.

Durham, W. B., W. L. Bourcier, and E. A. Burton (2001), Direct observation of reactive flow in a single fracture, *Water Resour. Res.*, *37*(1), 1–12.

Elsworth, D., and H. Yasuhara (2006), Short-timescale chemo-mechanical effects and their influence on the transport properties of fractured rock, *Pure Appl. Geophys.*, *163*, 2051–2070.

Gouze, P., C. Noiriel, C. Bruderer, D. Loggia, and R. Leprovost (2003), X-ray tomography characterization of fracture surfaces during dissolution, *Geophys. Res. Lett.*, *30*(5), 1267, doi:10.1029/2002GL016755.

Hanna, R. B., and H. Rajaram (1998), Influence of aperture variability on dissolutional growth of fissures in karst formations, *Water Resour. Res.*, *34*, 2843–2853.

Heidug, W. K. (1995), Intergranular solid-fluid phase transformations under stress: The effect of surface forces, *J. Geophys. Res.*, *100*, 5931–5940.

Kalia, N., and V. Balakotaiah (2009), Effect of medium heterogeneities on reactive dissolution of carbonates, *Chem. Eng. Sci.*, *64*, 376–390.

King, P. B. (1948), *Geology of the Southern Guadalupe Mountains, Texas, U. S. Geol. Survey Prof. Pap.*, 215, U. S. Geol. Survey, Tex.

Liu, J., J. Sheng, A. Polak, D. Elsworth, H. Yasuhara, and A. Grader (2006), A fully coupled hydrological-mechanical-chemical model for fracture sealing and preferential opening, *Int. J. Rock Mech. Min. Sci.*, *43*, 23–26.

Liu, X., A. Ormond, K. Bartko, Y. Li, and P. Ortoleva (1997), A geochemical reaction-transport simulator for matrix acidizing analysis and design, *J. Petrol. Sci. Eng.*, *17*, 181–196.

Manga, M., I. Beresnev, E. E. Brodsky, J. E. Elkhoury, D. Elsworth, S. E. Ingebritsen, D. C. Mays, and C.-Y. Wang (2012), Change in permeability caused by transient stresses: Field observations, experiments, and mechanisms, *Rev. Geophys.*, *50*, 2, doi:10.1029/2011RG000382.

Nemoto, K., N. Watanabe, N. Hirano, and N. Tsuchiya (2009), Direct measurement of contact area and stress dependence of anisotropic flow through rock fracture with heterogeneous aperture distribution, *Earth Planet. Sci. Lett.*, *281*, 81–87.

Noiriel, C., B. Made, and P. Gouze (2007), Impact of coating development on the hydraulic and transport properties in argillaceous limestone fracture, *Water Resour. Res.*, *43*, W09406, doi:10.1029/2006WR005379.

Noort, R. V., and C. J. Spiers (2009), Kinetic effects of microscale plasticity at grain boundaries during pressure solution, *J. Geophys. Res.*, *114*, B03206, doi:10.1029/2008JB005634.

Palmer, A. N. (1991), Origin and morphology of limestone caves, *Geol. Soc. Am. Bull.*, *103*, 1–21.

Panga, M., M. Ziauddin, and V. Balakotaiah (2005), Two-scale continuum model for simulation of wormholes in carbonate acidization, *AIChE J.*, *51*, 3231–3248.

Polak, A., D. Elsworth, H. Yasuhara, A. S. Grader, and P. M. Halleck (2003), Permeability reduction of a natural fracture under net dissolution by hydrothermal fluids, *Geophys. Res. Lett.*, *30*(20), 2020, doi:10.1029/2003GL017575.

Polak, A., D. Elsworth, J. Liu, and A. S. Grader (2004), Spontaneous switching of permeability changes in a limestone fracture with net dissolution, *Water Resour. Res.*, *40*, W03502, doi:10.1029/2003WR002717.

Plummer, L. N., T. M. L. Wigley, and D. L. Parkhurst (1978), The kinetics of calcite dissolution in CO2-Water systems at 5 to 60°C and 0.0 to 1.0 atm CO2, *Am. J. Sci.*, *278*, 179–216.

Revil, A. (1999), Pervasive pressure-solution transfer: A poro-visco-plastic model, *Geophys. Res. Lett.*, *26*(2), 255–258.

Rutter, E. H. (1976), The kinetic of rock deformation by pressure solution, *Philos. Trans. R. Soc. A*, *283*, 203–219.

Stephenson, L. P., W. J. Plumley, and V. V. Palciauskas (1992), A model for sandstone compaction by graing interpenetration, *J. Sediment. Petrol.*, *62*, 11–22.

Szymczak, P., and A. J. C. Ladd (2004), Microscopic simulations of fracture dissolution, *Geophys. Res. Lett.*, *31*, L23606, doi:10.1029/2004GL021297.

Szymczak, P., and A. J. C. Ladd (2009), Wormhole formation in dissolving fractures, *J. Geophys. Res.*, *114*, B06203, doi:10.1029/2008JB006122.

Taron, J., and D. Elsworth (2010), Constraints on compaction rate and equilibrium in the pressure solution creep of quartz aggregates and fractures: Controls of aqueous concentration, *J. Geophys. Res.*, *115*, B07211, doi:10.1029/2009JB007118.

Tsang, C. F. (1991), Coupled hydromechanical-thermochemical processes in rock fracture, *Rev. Geophys.*, *29*(4), 537–551.

Tokunaga, K. T. (2011), Physicochemical controls on adsorbed water film thickness in unsaturated geological media, *Water Resour. Res.*, *47*, W08514, doi:10.1029/2011WR010676.

Watanabe, N., N. Hirano, and N. Tsuchiya (2009), Diversity of channeling flow in heterogeneous aperture distribution inferred from integrated experimental-numerical analysis on flow through shear fracture in granite, *J. Geophys. Res.*, *114*, B04208, doi:10.1029/2008JB005959.

Wigley, T. M. L., and L. N. Plummer (1976), Mixing of carbonate waters, *Geochim. Cosmochim. Acta*, *40*, 989–975.

Yasuhara, H., D. Elsworth, and A. Polak (2004), Evolution of permeability in a natural fracture: Significant role of pressure solution, *J. Geophys. Res.*, *109*, B03204, doi:10.1029/2003JB002663.

Yasuhara, H., A. Polak, Y. Mitani, A. G. Grader, P. M. Halleck, and D. Elsworth (2006a), Evolution of fracture permeability through fluid-rock reaction under hydrothermal conditions, *Earth Planet. Sci. Lett.*, *244*, 186–200.

Yasuhara, H., D. Elsworth, A. Polak, J. Liu, A. Grader, and P. Halleck (2006b), Spontaneous switching between permeability enhancement and degradation in fractures in carbonate: Lumped parameter representation of mechanically- and chemically-mediated dissolution, *Transp. Porous Media*, *65*, 385–409, doi:10.1007/s11242-006-6386-2.